RSC Advances

PAPER

View Article Online
View Journal | View Issue

Cite this: *RSC Adv.*, 2022, **12**, 17422

Transport properties of $MoS_2/V_7(Bz)_8$ and graphene/$V_7(Bz)_8$ vdW junctions tuned by bias and gate voltages†

Hong Yu,[a] Danting Li,[a] Yan Shang,[a] Lei Pei,[a] Guiling Zhang,*[a] Hong Yan*[a] and Long Wang[b]

The $MoS_2/V_7(Bz)_8$ and graphene/$V_7(Bz)_8$ vdW junctions are designed and the transport properties of their four-terminal devices are comparatively investigated based on density functional theory (DFT) and the nonequilibrium Green's function (NEGF) technique. The MoS_2 and graphene nanoribbons act as the source-to-drain channel and the spin-polarized one-dimensional (1D) benzene–V multidecker complex nanowire ($V_7(Bz)_8$) serves as the gate channel. Gate voltages applied on $V_7(Bz)_8$ exert different influences of electron transport on $MoS_2/V_7(Bz)_8$ and graphene/$V_7(Bz)_8$. In $MoS_2/V_7(Bz)_8$, the interplay of source and gate bias potentials could induce promising properties such as negative differential resistance (NDR) behavior, output/input current switching, and spin-polarized currents. In contrast, the gate bias plays an insignificant effect on the transport along graphene in graphene/$V_7(Bz)_8$. This dissimilarity is attributed to the fact that the conductivity follows the sequence of MoS_2 < $V_7(Bz)_8$ < graphene. These transport characteristics are examined by analyzing the conductivity, the currents, the local density of states (LDOS), and the transmission spectra. These results are valuable in designing multi-terminal nanoelectronic devices.

Received 5th April 2022
Accepted 6th June 2022

DOI: 10.1039/d2ra02196j

rsc.li/rsc-advances

1. Introduction

Two-dimensional (2D) materials have become the up-to-date focal point of research in past decades owing their prominent electronic, optical, and magnetism properties, which are used in wide fields from field effect transistors (FETs),[1–3] optoelectronics,[4–7] to spintronics.[8–10] As the brightest star in the 2D material family, graphene has attracted constant academic and individual research interest and enthusiasm.[11–17] Inspired by these pioneering works, various kinds of 2D materials, for example, 2D transition metal dichalcogenides (TMDs),[18–22] have sprung up and become research hotspots. Among TMDs, MoS_2 nanosheets have drawn special attention due to their high stability, good semi-conductivity, large surface, *etc.*, which are desirable in nano electronic devices.[23] In recent years, numerous efforts have been devoted to fabricate van der Waals (vdW) heterojunctions of 2D materials by stacking alien components using various chemical techniques for engineering expected and improved properties toward practical applications.[24–31] The carrier mobility of 2D materials can be retained from vdW interactions, since it does not destroy the bonding properties in intralayers. The interlayer coupling between the two vdW-stacked 2D layers can result in novel physical properties. Many theoretical works have focused on studying the transport properties of these 2D heterojunctions by constructing two-terminal devices. However, in experiments, electron transport is usually measured using a four-probe apparatus.[32–37] On the other hand, for most practical applications, multi-terminal electronic devices are needed. Therefore, it is highly necessary to theoretically investigate the transport properties of multi-terminal devices, which is still less studied to date.

Simultaneously, with the approaching physical limit of silicon based transistors, seeking emerging device architectures and new electronic materials has become an essential topic to meet the Moore's law. Recently, spintronic devices have received extensive attentions due to the combined merits of the electron transporting, the magnetic moment, and the electron spin. Therefore, introducing spin-polarized component into 2D materials to construct vdW heterojunctions is anticipated to be an effective strategy to explore novel functional materials with desirable properties.[38–41] However, as far as we know, studies on the spin-polarized 2D vdW heterojunctions are still scarce from both experimental and theoretical points of view. The one-dimensional (1D) benzene–V multidecker complexes nanowire, $V_n(Bz)_m$, not only has been successfully synthesized from

[a]*School of Materials Science and Chemical Engineering, Harbin University of Science and Technology, Harbin 150040, P. R. China. E-mail: guiling-002@163.com; yanhong204821@aliyun.com*

[b]*HeiLongJiang Construction Investment Group Co. Ltd, No. 523, Sanda Dongli Road, Harbin, 150040, P. R. China*

† Electronic supplementary information (ESI) available. See https://doi.org/10.1039/d2ra02196j

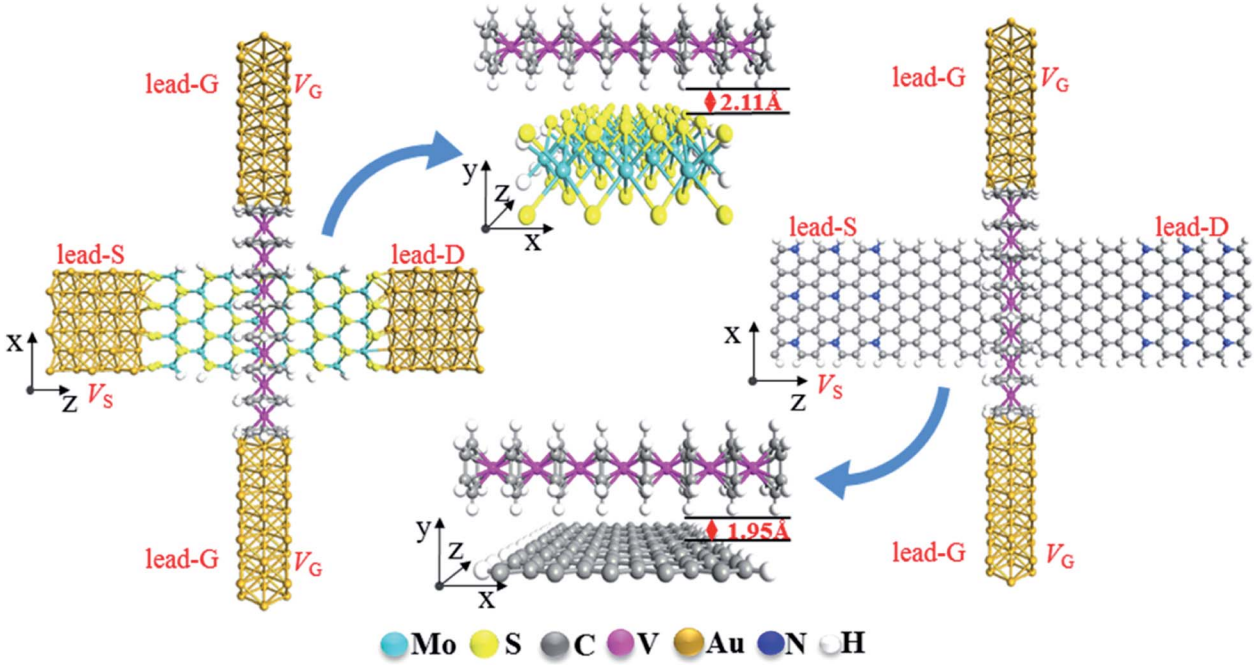

Fig. 1 Schematic plots of $MoS_2/V_7(Bz)_8$ and Graphene/$V_7(Bz)_8$ four-terminal devices. Where lead-S, lead-D, and lead-G represent the source, drain, and gate leads, respectively. V_S and V_G represent the bias voltage applied on lead-S and the gate voltage applied on lead-G, respectively.

reaction of laser-vaporized metal atoms with C_6H_6 in a He atmosphere, but also have been imaged or detected using scanning tunneling microscopy (STM), UV–vis and IR, electron paramagnetic resonance (EPR), time-of-flight mass spectroscopies, and photoionization spectroscopies.[42–45] Experimental works as well as theoretical studies have confirmed that the unpaired electrons on the V atoms are coupled ferromagnetically (FM), and also suggest that the ground state of $V_n(Bz)_m$ exhibits half-metallicity and spin filter effect.[44,46]

Further onward, stimulated by the splendor work on MoS_2 transistors using a single-walled carbon nanotube as the gate electrodes to tune the transport properties,[47] we construct four-terminal devices for MoS_2 and graphene heterojunctions: MoS_2 and graphene are connected to the source and drain leads, while the spin polarized $V_n(Bz)_m$ nanowire serves as gate terminals. Bias voltages and gate voltages are applied on the source lead and gate lead, respectively. The synergistic tuning effects of the bias and gate voltages on transport properties of MoS_2 and graphene are investigated by employing the density functional theory (DFT) with non-equilibrium Green's function (NEGF) methodology.

2. Models and computational methods

Fig. 1 shows the structures of the four-terminal devices for $MoS_2/V_7(Bz)_8$ and graphene/$V_7(Bz)_8$ vdW heterojunctions. MoS_2

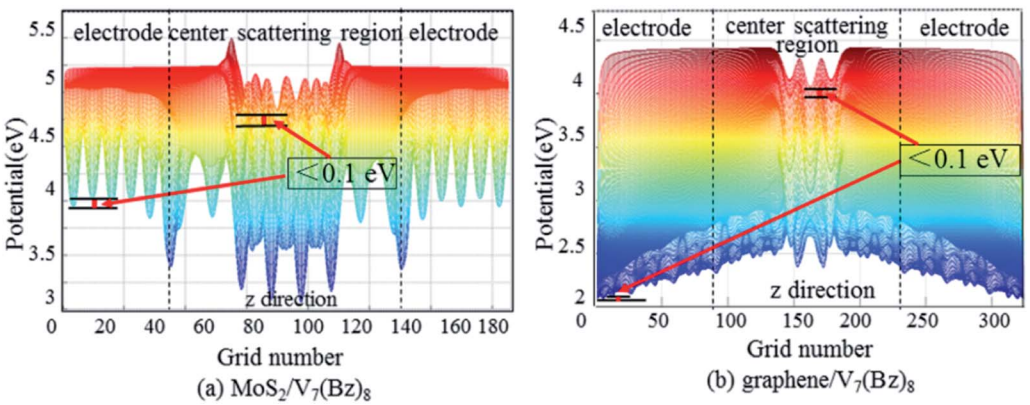

Fig. 2 The calculated potential distribution of the buffers near the leads in the two four-terminal devices, (a) is that in $MoS_2/V_7(Bz)_8$ device and (b) is that in graphene/$V_7(Bz)_8$ device.

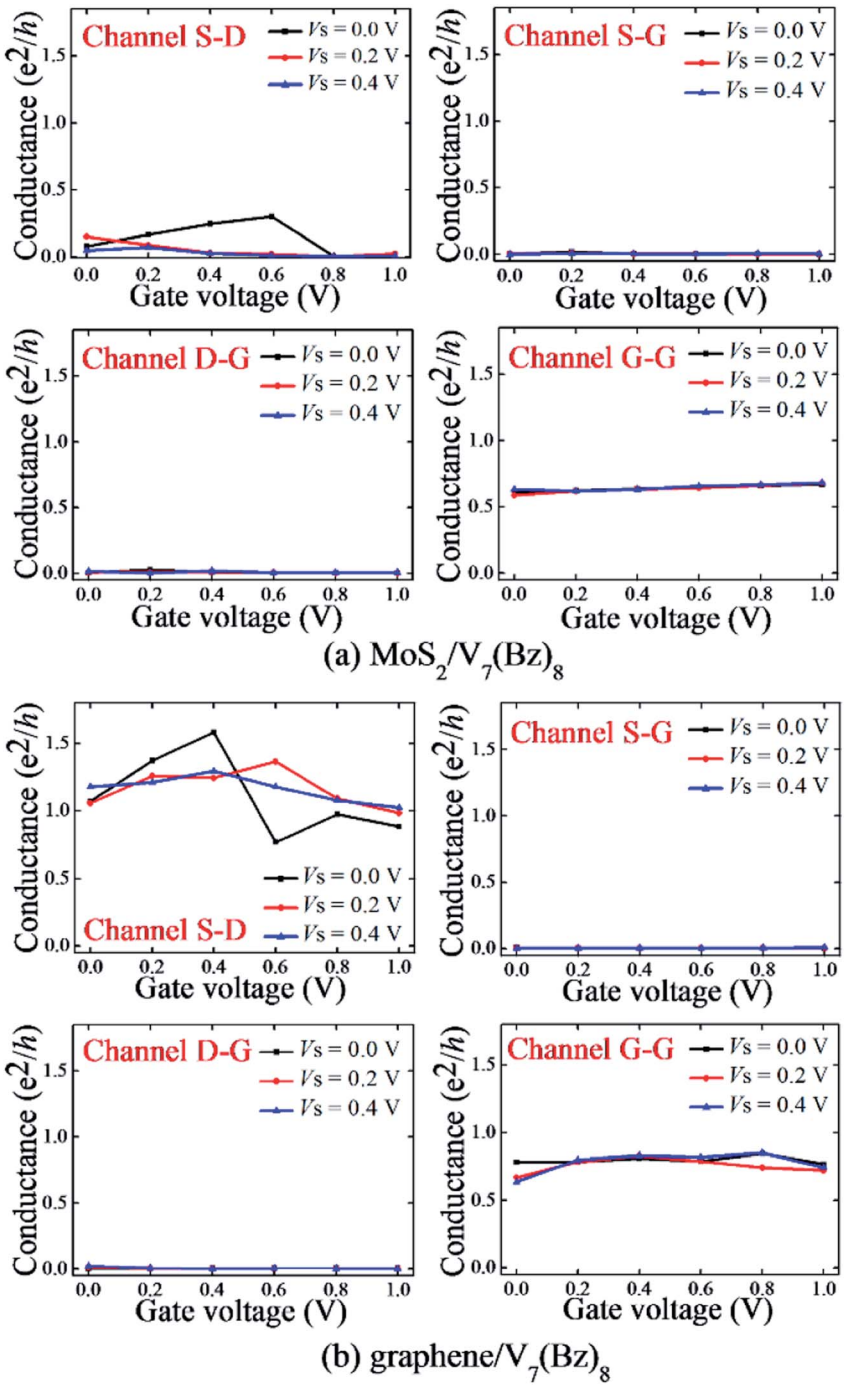

Fig. 3 Conductance for channel S–D, channel S–G, channel D–G, and channel G–G as a function of V_G at fixed values of V_S = 0.0, 0.2, or 0.4 V of the four-terminal $MoS_2/V_7(Bz)_8$ and graphene/$V_7(Bz)_8$ devices. (a and b) Are for the $MoS_2/V_7(Bz)_8$ and graphene/$V_7(Bz)_8$ devices, respectively.

and graphene offer the source-to-drain scatter region, and $V_7(Bz)_8$ nanowire provides the gate channel. For the sake of simplicity, the leads are denoted as lead-S, lead-D, and lead-G for the source, drain, and gate leads, respectively. The source-to-drain direction is defined as the z direction, and the gate to gate direction is referred as the x direction. The MoS_2 and graphene are placed in the $x \times z$ plane. The MoS_2 scatter region contains 9-layered S and 8-layered Mo in the z direction, as well as 4-layered S and 3-layered Mo in the x direction, which extends a 11.33 Å × 21.90 Å ($x \times z$) plane. A similar size of graphene ribbon in the x and z direction (11.07 Å × 19.89 Å) is tailored as the scatter region, too. Such scatter region is long enough in the z direction to ignore the interaction between lead-S and lead-D. This can be confirmed by the small potential changes near the electrodes (<0.1 eV) calculated for the two devices (Fig. 2). Every dangling bonds at edges are saturated by H atoms to stabilize

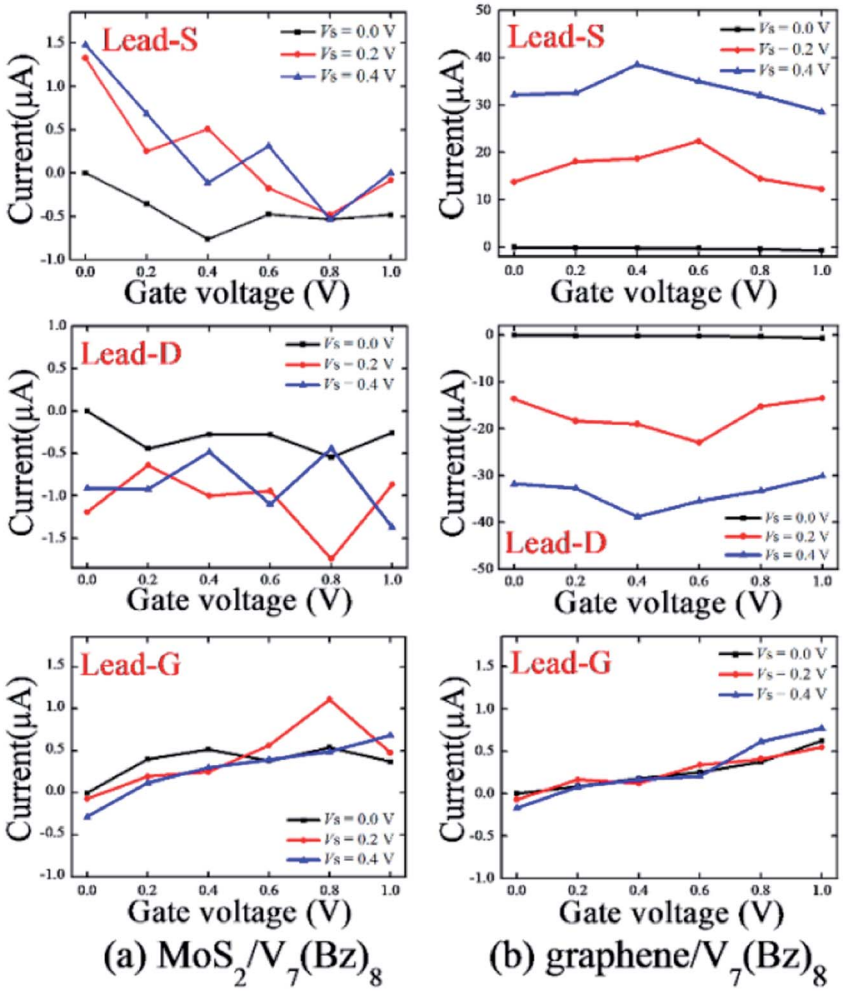

Fig. 4 Total currents for lead-S, lead-D, and lead-G as a function of V_G at fixed values of V_S = 0.0, 0.2, or 0.4 V of the four-terminal devices, where (a) shows those in $MoS_2/V_7(Bz)_8$ devices, and (b) is in graphene/$V_7(Bz)_8$.

the system. The $V_7(Bz)_8$ nanowire overlies the center of MoS_2 and graphene surfaces with a vdW distance from them, and its longitudinal axis is parallel to the x direction and perpendicular to the z direction. Each lead-G in $MoS_2/V_7(Bz)_8$ and graphene/$V_7(Bz)_8$ is modeled by a Au(100)-(3 × 3) surface with 8 layers. The Au–C distance is set to be 2.05 Å based on their covalent radius.[48] MoS_2 is semi-conductor, so we use Au(100)-(6 × 3) surfaces with 5 layers as the lead-S and lead-D for $MoS_2/V_7(Bz)_8$. As the S atom has good affinity with the gold surface, dithiolate derivatives have been used for the construction of metal/scatter region/metal devices in general.[49–51] Therefore, in the present work, we also use the S atom layer of MoS_2 to link the Au electrodes. The S–Au distance was set as 2.34 Å according to the reported literature.[52] To ensure that the bonds match well between graphene and leads, we elongate the graphene additionally by 31.26 Å as the lead-S and lead-D. Since graphene nanoribbon is semi-conductor along the armchair direction, we use the N atoms to dope the graphene lead-S and lead-D since the N atoms can introduce additional π electrons to make the two leads become conductor.[53,54] A vacuum of 20 Å in y direction is involved to eliminate the coupling between adjacent images.

The DFT method with generalized gradient approximation (GGA) implemented in ATK package is employed to optimize the four-terminal structures. For both $MoS_2/V_7(Bz)_8$ and graphene/$V_7(Bz)_8$ four-terminal devices, all the leads are frozen and the scatter regions are optimized. The self-consistent total energies are converged to 10^{-4} eV and the forces are converged to 0.05 eV $Å^{-1}$. The optimized cartesian coordinates of all the models are given in Tables S1 and S2 in the ESI.† The optimized distance is 2.11 Å from MoS_2 to $V_7(Bz)_8$ and 1.95 Å from graphene to $V_7(Bz)_8$, a typical vdW interaction. Then, the transport properties of the optimized devices are calculated using DFT with NEGF methodology within Nanodcal software package.[55,56] The linear combination of atomic orbitals (LCAO) is employed to expand physical parameters. The standard nonlocal norm-conserving pseudopotentials is used to describe the atomic core, and the double-zeta polarized (DZP) basis set is for valence electronic orbitals.[57,58] The exchange-correlation function is considered by the local density approximation (LDA).[58,59] The k-point for the central region is meshed as 1 × 1 × 1 (x × y × z), and that is 1 × 1 × 100 for lead-S and lead-D, 100 × 1 × 1 for lead-G. It is worth noting that, in all calculations the spin of V

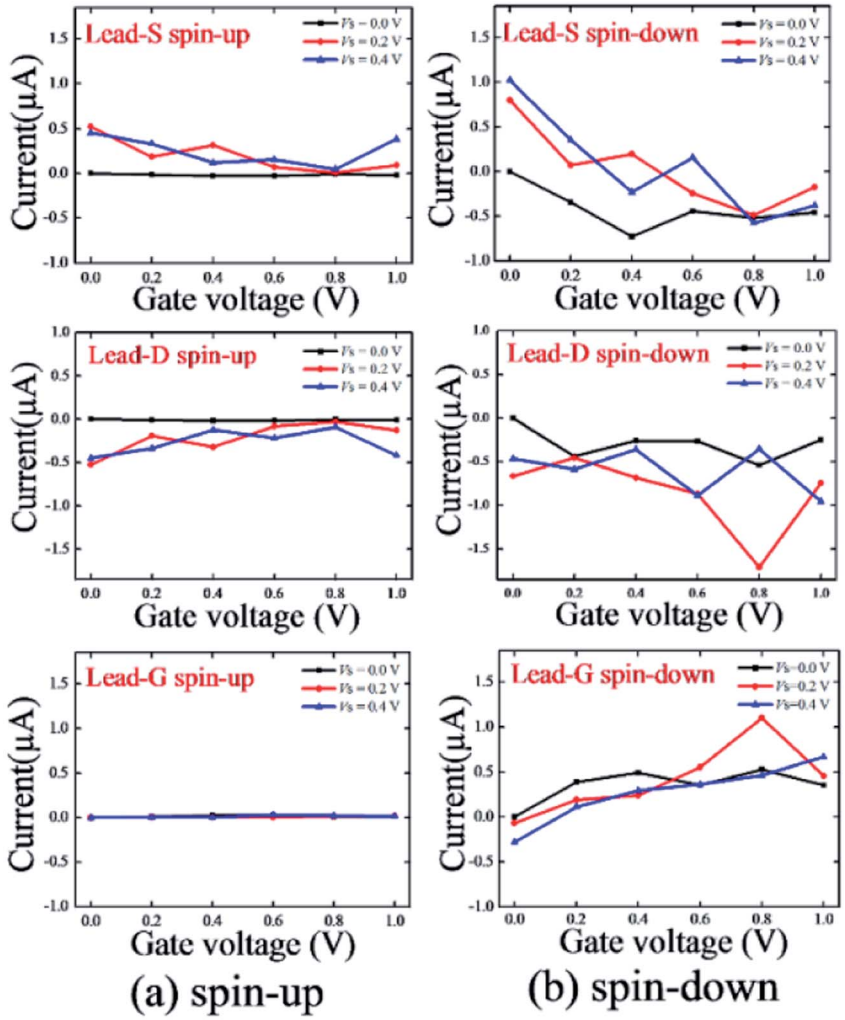

Fig. 5 Spin currents for lead-S, lead-D, and lead-G as a function of V_G at fixed values of $V_S = 0.0$, 0.2, or 0.4 V of the four-terminal $MoS_2/V_7(Bz)_8$ device. (a) Depicts the spin-up states of $MoS_2/V_7(Bz)_8$, and (b) depicts those for spin-down state, respectively.

atoms is considered by using LAD + U scheme, and the U–J is set as 3.0 eV.[60] 160 Rydberg cutoff energy is applied.

The spin-dependent current in leads for multi-terminal system can be obtained using the Landauer–Büttiker formula (1):[57,61,62]

$$I_\sigma = \frac{e}{h}\sum_\beta \int_{-\infty}^{+\infty} dE T_{\alpha\beta}(E, V_\alpha, V_\beta)\left[f_\beta(E) - f_\alpha(E)\right] \quad (1)$$

where f_α (f_β) describes the Fermi distribution functions of lead-α (lead-β). V_α (V_β) is the bias voltages applied on lead-α (lead-β). $\sigma \equiv \uparrow, \downarrow$ is the spin index. The transmission coefficient $T_{\alpha\beta}$ between lead-α and lead-β is dependent on E, V_α, and V_β. And the total current is $I = I\uparrow + I\downarrow$.

Considering the multi-terminals, the conductance between lead-α and lead-β can be evaluated by formula (2):

$$G_{\alpha\beta} = \frac{e^2}{h} T_{\alpha\beta}(E) \quad (2)$$

3. Results and discussion

In this section, we mainly document on how the bias voltage (V_S) and the gate voltage (V_G) synergistically influence the transport properties of $MoS_2/V_7(Bz)_8$ and graphene/$V_7(Bz)_8$ vdW junctions from the aspects of conductance, currents, LDOS, and transmission. The V_S is set as 0.0, 0.2, 0.4 V, respectively. And at each certain V_S, the V_G ranges from 0.0 to 1.0 V by a step of 0.2 V.

3.1 Conductivity

To convenient description, the channels between any two terminals are denoted as channel S–D, channel S–G, channel D–G, and channel G–G.

Fig. 3 shows the calculated conductance of each channel of $MoS_2/V_7(Bz)_8$ and graphene/$V_7(Bz)_8$ devices with the variation of V_S and V_G. For the sake of comparison, the scales of conductance in vertical-axle in Fig. 3 are the same for all the channels, and Fig. S1† with adapted vertical-axis scales is supplied as

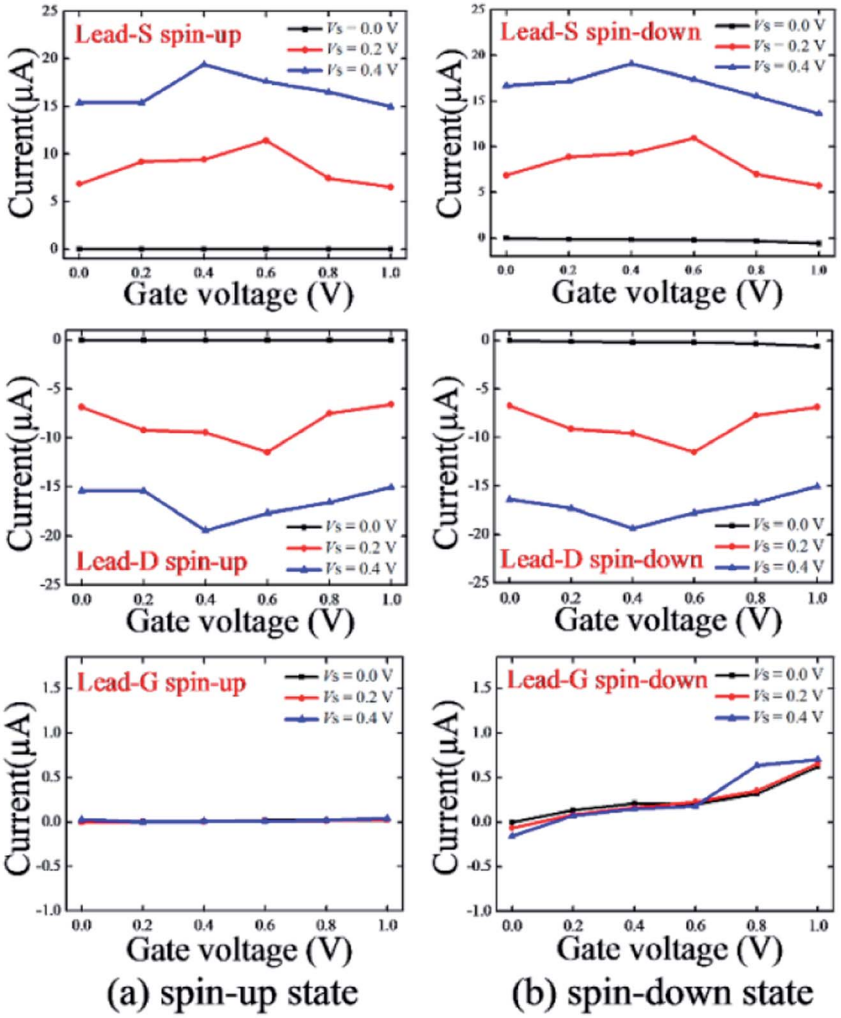

Fig. 6 Spin currents for lead-S, lead-D, and lead-G as a function of V_G at fixed values of V_S = 0.0, 0.2, or 0.4 V of the four-terminal graphene/$V_7(Bz)_8$ device. (a) Depicts the spin-up states, and (b) depicts those for spin-down state, respectively.

ESI.† The conductance is bigger than $0.8e^2/h$, in the range of $0.5–1.0e^2/h$, and smaller than $0.3e^2/h$ for graphene channel S–D, $V_7(Bz)_8$ channel G–G, and MoS_2 channel S-D, respectively. That is, the conductivity follows the sequence of MoS_2 < $V_7(Bz)_8$ < graphene. Therefore, using $V_7(Bz)_8$ as gate may play different effects on tuning electron transporting through MoS_2 and graphene. Since the $V_7(Bz)_8$ nanowire attaches to MoS_2 and graphene *via* vdW interaction, the conductance of channels S–G and D–G are very small (<$0.03e^2/h$). The potentials from gate and from source couple in different degrees in $MoS_2/V_7(Bz)_8$ and graphene/$V_7(Bz)_8$ under various V_S and V_G. This integrates the change of resistance from source to drain, which makes the conductance goes up or down.

3.2 Current

To further understand the transport property of the four-terminal devices, we calculated the total currents, I_S, I_D, and I_G, passing through lead-S, lead-D, and lead-G, respectively. Currents from lead to center region are input and defined as positive values, while those from center region to lead are output and appointed as negative values.

Fig. 4 displays the total currents through the leads with the variation of V_S and V_G applied on $MoS_2/V_7(Bz)_8$ and graphene/$V_7(Bz)_8$ devices. Multi-channels in four-terminal devices could cause complicated transport properties aroused from the intricacy of channel couplings. Actually, the magnitude of each lead current comes from the synergistic action of all pathways. For example, though lead-S current is directly related to channels S–D and S–G, channels S–D and S–G are simultaneously influenced by channels D–G and G–G.

Now we consider the total currents, I_S, I_D, and I_G of $MoS_2/V_7(Bz)_8$ device (Fig. 4a). With free gate voltage, a small amount of current leaks off lead-G when applied V_S = 0.2 and 0.4 V, while the lead-G current becomes input once V_G imposed, which could exert considerable effect on the source-to-drain transporting. The lead-D currents are always output owing to its low voltage potential compared with other three leads. At V_S = 0.0 V, lead-S and lead-D give output currents with the absolute values of I_S < 1.0 μA and I_D < 0.5 μA, which are induced by the applied gate

Table 1 Local density of states (LDOS) of the four-terminal $MoS_2/V_7(Bz)_8$ and graphene/$V_7(Bz)_8$ devices at various V_G exemplified by $V_S = 0.2$ V

	LDOS at $V_S = 0.2$ V			
	$MoS_2/V_7(Bz)_8$ device		Graphene/$V_7(Bz)_8$ device	
V_G (V)	Spin-up	Spin-down	Spin-up	Spin-down
0.0	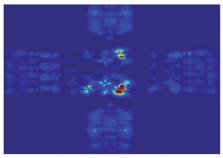	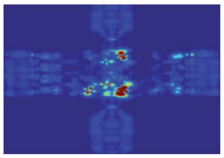	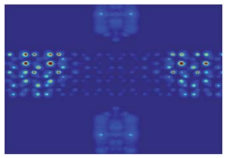	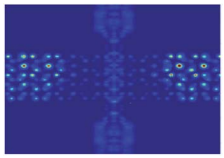
0.2	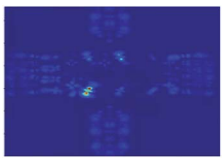	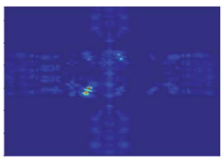	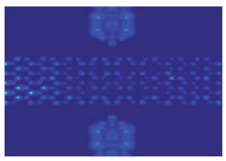	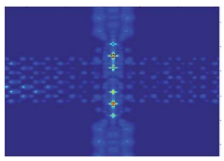
0.4	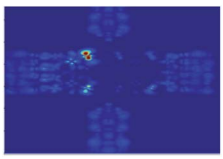	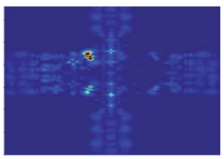	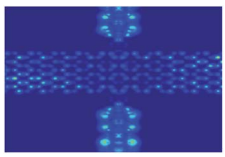	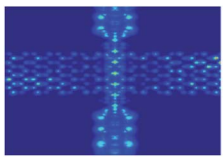
0.6	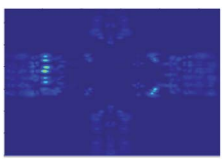	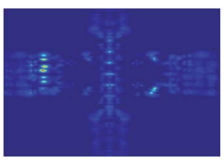	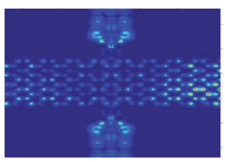	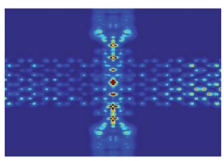
0.8	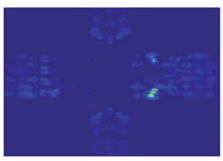	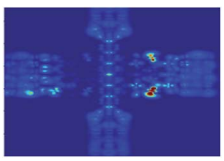	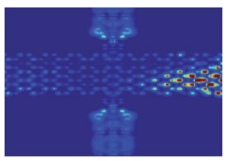	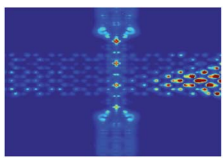
1.0	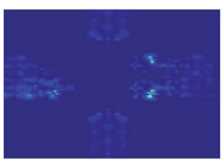	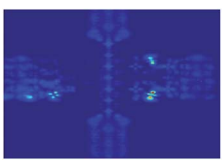	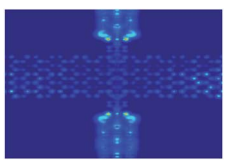	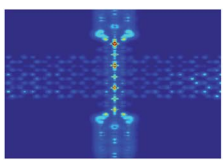

voltages. Interestingly, regardless of any V_S, the I_S, I_D, and I_G curves present a pattern of up and down oscillation with the changing of V_G, resulting in NDR peaks. Of course, the magnitude, the position, and the numbers of these NDR peaks are different for different leads at various V_S and V_G. In fact, conductivity, as a complicated phenomenon, relates to comprehensive factors such as scatter region structure, scatter region–lead interaction, couplings between channels, changes of resistance induced by voltages, *etc.* For example, the asymmetric character of MoS_2 structure not only induces different resistance for different channels, but also induces different left and right MoS_2–lead interactions. Therefore, at zero V_S bias, the I_S and I_D curves give different shapes. All these comprehensive factors may also be responsible for the dissimilarity of the NDR behaviors of I_S, I_D, and I_G. When nonzero V_S is applied, as the V_G increases, the input I_S current decreases as a whole and could switches to output at certain V_G, *e.g.*, at $V_G = 0.6$ V for $V_S = 0.2$ V and at $V_G = 0.4$ and 0.8 V for $V_S = 0.4$ V. Therefore, the currents across lead-S are rather dependent on the interplay of V_S and V_G. At $V_S = 0.2$ and 0.4 V, the absolute values of I_D rise comparing with $V_S = 0.0$ V. This is a reasonable result from the higher potential injected into the channel S–D. The magnitude of the output currents of lead-D tends to be balanced around 1.0 μA. All these properties are much desirable for designing functional devices with fascinating characteristics such as NDR behavior and input/output switching.

As to the graphene/$V_7(Bz)_8$ device, the total currents of I_S, I_D, and I_G display a much different feature from $MoS_2/V_7(Bz)_8$ as shown from Fig. 4b. Intuitively, the gate V_G plays a small role on the carries transport *via* the graphene plane. This result can be deduced from two phenomena: one is that the magnitudes of I_S and I_D (10–40 μA) are much higher than I_G (<1.0 μA) under applied V_G; another is that the input values of I_S are almost

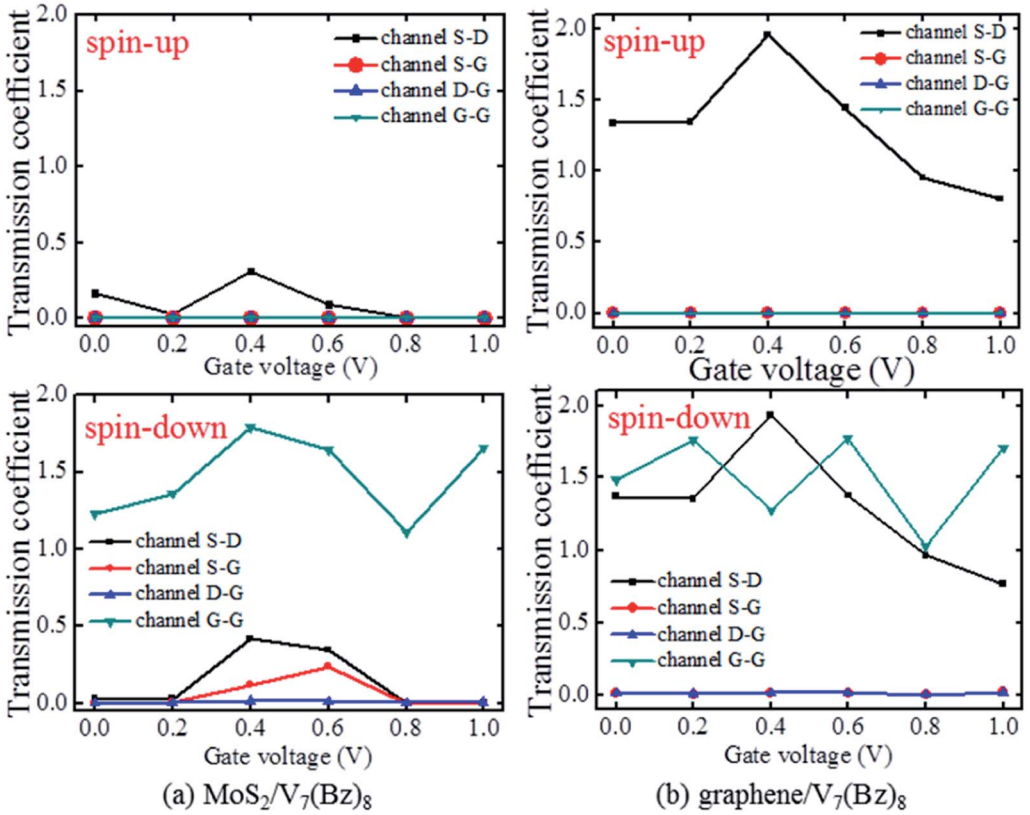

Fig. 7 Transmission coefficient of all channels in two devices with variational V_G from 0.0 to 1.0 V at $V_S = 0$ V. (a) Shows spin-up and spin-down state in $MoS_2/V_7(Bz)_8$ device, and (b) is that for graphene/$V_7(Bz)_8$ device.

equal to the output data of I_D at given V_S and V_G, indicating that the injected I_S almost arrives to the lead-D completely. No evident NDR behavior is observed for graphene/$V_7(Bz)_8$. In addition, unlike in $MoS_2/V_7(Bz)_8$ which there exists input/output switching of lead-S, the current of lead-S in graphene/$V_7(Bz)_8$ is always input within the considered gate bias. The reason for these different phenomena between $MoS_2/V_7(Bz)_8$ and graphene/$V_7(Bz)_8$ lies in the fact that graphene has higher conductivity than MoS_2.

To investigate how the spin-polarized character of $V_7(Bz)_8$ influence the transport property of $MoS_2/V_7(Bz)_8$ and graphene/$V_7(Bz)_8$, we computed the spin-up currents, $I_{S\uparrow}$, $I_{D\uparrow}$, and $I_{G\uparrow}$ as well as the spin-down currents, $I_{S\downarrow}$, $I_{D\downarrow}$, and $I_{G\downarrow}$, for lead-S, lead-D, and lead-G, respectively. The results are plotted in Fig. 5 and 6 as a function of V_G at a given V_S.

As expected, for $V_7(Bz)_8$ in both two devices, the $I_{G\uparrow}$ remains nearly zero, while the $I_{G\downarrow}$ possesses the same magnitude to the total I_G. This thoroughly inherits the intrinsic spin-polarized feature of pure $V_7(Bz)_8$.[60,63] Quite significantly, the spin polarized feature of $V_7(Bz)_8$ induces different polarized transport property from $MoS_2/V_7(Bz)_8$ to graphene/$V_7(Bz)_8$. In the case of $MoS_2/V_7(Bz)_8$, spin-up and spin-down channels of lead-S and lead-G are split by the polarization property of $V_7(Bz)_8$. At $V_S = 0.0$ V, the spin-up paths of both lead-S and lead-D of $MoS_2/V_7(Bz)_8$ are closed with almost zero current, and the total currents I_S and I_D entirely come from the spin-down $I_{S\downarrow}$ and $I_{D\downarrow}$. This is mainly due to the fact that the spin-up channel of $V_7(Bz)_8$ is almost closed and hence cannot cause perturbation on the spin-up pathway of MoS_2. On the contrary, the spin-down state of $V_7(Bz)_8$ dominates electron transporting, enabling strong coupling with the spin-down channel of MoS_2. Under nonzero V_S, the currents through lead-S and lead-D in $MoS_2/V_7(Bz)_8$ are polarized by a large extent. For the spin-up state, the currents of $I_{S\uparrow}$ are all input and those of $I_{D\uparrow}$ are all output. Both $I_{S\uparrow}$ and $I_{D\uparrow}$ curves of $MoS_2/V_7(Bz)_8$ change smoothly in a small scale of 0.0–0.5 μA along the variation of V_G. In striking contrast, the spin-down currents of $I_{S\downarrow}$ and $I_{D\downarrow}$ fluctuate significantly with the changing of V_G, with a large range of from 1.0 to −0.5 μA for $I_{S\downarrow}$ and from 0.0 to −1.7 μA for $I_{D\downarrow}$. Observed carefully, one can find that the changing trends of $I_{S\downarrow}$ and $I_{D\downarrow}$ curves are roughly analogous to those of the total I_S and I_D. The NDR behavior and the input/output switch character of $MoS_2/V_7(Bz)_8$ are mainly dominated by the spin-down state. Now turn to graphene/$V_7(Bz)_8$, quite different from $MoS_2/V_7(Bz)_8$, no matter what V_S and V_G applied, the spin-up currents are almost equivalent to spin-down values for both lead-S and lead-D. Though the polarized characteristic of $V_7(Bz)_8$ is preserved in graphene/$V_7(Bz)_8$, its conductivity is too much weaker than graphene that can not exert valid influence on channel S–D.

3.3 Local density of states

Table 1 displays the computed local density of states (LDOS) results of two devices under $V_S = 0.2$ V, where the even LDOS

distribution suggests an effective transport channel. The scenario of the polarized transport behavior of $MoS_2/V_7(Bz)_8$ leads becomes more obvious by analyzing the LDOS distributions. As representative example, it is clear that the LDOS of the spin-down state of $V_7(Bz)_8$ delocalizes stronger than the spin-up state, which could bring about coupling with the spin-down state of MoS_2, and consequently, lead to the spin-polarized splitting of $MoS_2/V_7(Bz)_8$. The electronic potential on the whole system changes along with the relative magnitude of V_S and V_G, as can be reflected from the LDOS distributions. Clearly, charge carries in the spin-up state of either channel S–D or channel G–G are blocked more seriously than the spin-down state. As for the graphene/$V_7(Bz)_8$ device, the spin-down passage of $V_7(Bz)_8$ is open with uniform LDOS distribution while the spin-up path is closed with almost no LDOS. Despite of the maintained polarized character of $V_7(Bz)_8$, spin-up and spin-down channels along graphene has nearly identical LDOS spreading. This again demonstrates the unpolarized character of lead-S and lead-D currents.

3.4 Transmission coefficients and spectra

To further shed light on how the gate bias tune the transport property of $MoS_2/V_7(Bz)_8$ and graphene/$V_7(Bz)_8$ devices, we computed spin polarized transmission coefficients (TC) of each channel at the case of $V_S = 0.0$ V and V_G from 0.0 to 1.0 V, and the results are shown in Fig. 7.

Evidently, in both $MoS_2/V_7(Bz)_8$ and graphene/$V_7(Bz)_8$ devices, spin-down channel G–G composed of $V_7(Bz)_8$ has much higher TC than other channels, again demonstrating the preserved striking half-metallic character of $V_7(Bz)_8$. One can find that, in $MoS_2/V_7(Bz)_8$, the main channel S–D consisting of MoS_2 can not be largely influenced by the spin polarized character of the gate $V_7(Bz)_8$, as can be clearly seen from the comparable spin-up and spin-down TC. However, the spin polarized $V_7(Bz)_8$ directly consists of channels S–G and D–G, and thereby, it could induce spin split of channels S–G and D–G and generate larger spin-down TC than spin-up TC. Therefore, the spin polarized transport character of $MoS_2/V_7(Bz)_8$ mainly derives from the perturbation of the spin-down state of $V_7(Bz)_8$ upon the channels S–G and D–G. Regarding graphene/$V_7(Bz)_8$, charge carriers can easily flow from lead-S to lead-D since channel S–D has large TC, while other channels are almost closed with nearly zero TC except the spin-down channel G–G. In addition, spin-up and spin-down states of channel S–D display the same TC curves, illustrating the ignoring polarization influence of $V_7(Bz)_8$ on graphene.

Furtherly, we calculated the transmission spectra (TS) of the main channel S–D for $MoS_2/V_7(Bz)_8$ and graphene/$V_7(Bz)_8$

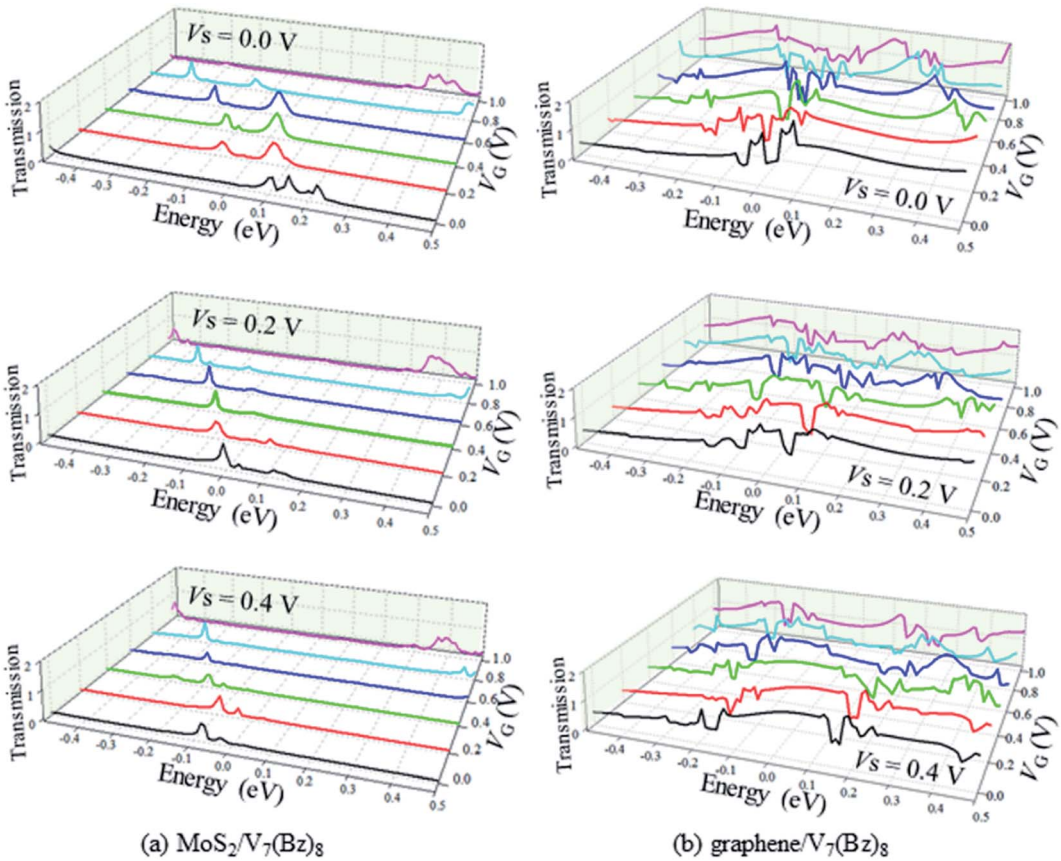

Fig. 8 Transmission spectra of channel S–D in $MoS_2/V_7(Bz)_8$ and graphene/$V_7(Bz)_8$ device with variational V_G from 0.0 to 1.0 V at a certain V_S, where (a) depicts the case in $MoS_2/V_7(Bz)_8$, and (b) is that for graphene/$V_7(Bz)_8$, respectively.

devices at each V_S and V_G, as plotted in Fig. 8. In the case of $MoS_2/V_7(Bz)_8$, at $V_S = 0.0$ V and $V_G = 0.0$ V, TS peak located above the E_f mainly arises from the native MoS_2. When adding V_G merely, an extra peak appears near the E_f owing to the gate carries injection into the channel S–D of $MoS_2/V_7(Bz)_8$. Once adding V_S together with V_G, only one peak exists below the E_f due to the suppression effect of the incoming V_G potential upon the V_S. Furthermore, with the increasing of V_G, such suppression effect in $MoS_2/V_7(Bz)_8$ becomes more significant, as the TS peak moves farer away from the E_f. In contrast, regardless of V_S and V_G, lots of TS peaks of channel S–D appear around the E_f of graphene/$V_7(Bz)_8$, again indicating the high conductivity of graphene.

4. Conclusion

The $MoS_2/V_7(Bz)_8$ and graphene/$V_7(Bz)_8$ vdW junctions are designed and the transport properties of their four-terminal devices are comparatively investigated based on the DFT and NEGF techniques. The MoS_2 and graphene nanoribbons act as the source-to-drain channel and the spin-polarized $V_7(Bz)_8$ nanowire serves as the gate channel. The transport characteristic is explored by investigating the conductance, currents, LDOS, and transmission spectra. Gate voltages applied on $V_7(Bz)_8$ exert different influences of electron transporting on $MoS_2/V_7(Bz)_8$ and graphene/$V_7(Bz)_8$. The interplay of source and gate bias potentials generates a pronounced influence on the transport property of $MoS_2/V_7(Bz)_8$. Evident NDR behavior, input/output current switches, as well as spin-polarized currents are found for $MoS_2/V_7(Bz)_8$. In contrast, the gate bias plays insignificant effect on the transporting along graphene. These results are promising in designing multi-terminal nanoelectronic devices.

Conflicts of interest

There are no conflicts of interest to declare.

Acknowledgements

This work was supported by the National Natural Science Foundation of China (Grant No. 51973046). And more, We gratefully acknowledge HZWTECH for providing computation facilities.

References

1 Q. Lv, F. Yan, N. Mori, W. Zhu, C. Hu, Z. R. Kudrynskyi, Z. D. Kovalyuk, A. Patane and K. Wang, Interlayer band-to-band tunneling and negative differential resistance in van der Waals BP/InSe field-effect transistors, *Adv. Funct. Mater.*, 2020, **30**, 1910713.

2 B. Jiang, X. Zou, J. Su, J. Liang, J. Wang, H. Liu, L. Feng, C. Jiang, F. Wang, J. He and L. Liao, Impact of thickness on contact issues for pinning effect in black phosphorus field-effect transistors, *Adv. Funct. Mater.*, 2018, **28**, 1801398.

3 W. Ahmad, Y. N. Gong, G. Abbas, K. Khan, M. Khan, G. Ali, A. Shuja, A. K. Tareen, Q. Khan and D. L. Li, Evolution of low-dimensional material-based field-effect transistors, *Nanoscale*, 2021, **13**, 5162.

4 J. L. Du, H. H. Yu, B. S. Liu, M. Y. Hong, Q. L. Liao, Z. Zhang and Y. Zhang, Strain engineering in 2d material-based flexible optoelectronics, *Small Methods*, 2020, **5**, 2000919.

5 Z. X. Li, D. Y. Li, H. Y. Wang, P. Chen, L. J. Pi, X. Zhou and T. Y. Zhai, Intercalation strategy in 2D materials for electronics and optoelectronics, *Small Methods*, 2021, **5**, 2100567.

6 Y. K. Liao, Z. F. Zhang, Z. B. Gao, Q. K. Qian and M. Y. Hua, Tunable properties of novel Ga_2O_3 monolayer for electronic and optoelectronic applications, *ACS Appl. Mater. Interfaces*, 2020, **12**, 30659–30669.

7 E. Singh, P. Singh, K. S. Kim, G. Y. Yeom and H. S Nalwa, Flexible molybdenum disulfide (MoS_2) atomic layers for wearable electronics and optoelectronics, *ACS Appl. Mater. Interfaces*, 2019, **11**, 11061–11105.

8 Y. P. Liu, C. Zeng, J. H. Zhong, J. N. Ding, Z. M. Wang and Z. W. Liu, Spintronics in two-dimensional materials, *Nano-Micro Lett.*, 2020, **12**, 93.

9 C. K. Safeer, J. Ingla-Aynés, F. Herling, J. H. Garcia, M. Vila, N. Ontoso, M. R. Calvo, S. Roche, L. E. Hueso and F. Casanova, Room temperature spin Hall effect in graphene/MoS_2 van der Waals heterostructures, *Nano Lett.*, 2019, **19**, 1074–1082.

10 A. Avsar, H. Ochoa, F. Guinea, B. Ozyilmaz, B. J. Van Wees and I. J. Vera-Marun, Colloquium: spintronics in graphene and other two-dimensional materials, *Rev. Mod. Phys.*, 2020, **92**, 021003.

11 A. P. Johnson, C. Sabu, N. K. Swamy, A. Anto, H. V. Gangadharappa and K. Pramod, Graphene nanoribbon: an emerging and efficient flat molecular platform for advanced biosensing, *Biosens. Bioelectron.*, 2021, **184**, 113245.

12 Y. J. Gao, J. L. Chen, G. R. Chen, C. H. Fan and X. G. Liu, Recent progress in the transfer of graphene films and nanostructures, *Small Methods*, 2021, **5**, 2100771.

13 S. Achra, T. Akimoto, J. F. de Marneffe, S. Sergeant, X. Y. Wu, T. Nuytten, S. Brems, I. Asselberghs, Z. Tokei and K. Ueno, Enhancing interface doping in graphene-metal hybrid devices using H-2 plasma clean, *Appl. Surf. Sci.*, 2021, **538**, 148046.

14 K. M. Wyss, D. X. Luong and J. M. Tour, Large-scale syntheses of 2d materials: flash joule heating and other methods, *Adv. Mater.*, 2022, **34**, 2106970.

15 I. Alcón, G. Calogero, N. Papior and M. Brandbyge, Electrochemical control of charge current flow in nanoporous graphene, *Adv. Funct. Mater.*, 2021, **31**, 2104031.

16 T. Chen, W. C. Ding, H. L. Li and G. H. Zhou, Length-independent multifunctional device based on penta-tetra-pentagonal molecule: a first-principles study, *J. Mater. Chem. C*, 2021, **9**, 3652.

17 Q. Sun, X. L. Yao, O. Groning, K. Eimre, C. A. Pignedoli, K. Muellen, A. Narita, R. Fasel and P. Ruffieux, Coupled spin states in armchair graphene nanoribbons with asymmetric zigzag edge extensions, *Nano Lett.*, 2020, **20**, 6429–6436.

18 P. L. Zhao, J. Yu, H. Zhong, M. Rosner, M. I. Katsnelson and S. J. Yuan, Electronic and optical properties of transition metal dichalcogenides under symmetric and asymmetric field-effect doping, *New J. Phys.*, 2020, **22**, 083072.

19 S. Y. Seo, D. H. Yang, G. Moon, O. F. N. Okello, M. K. Park, S. H. Lee, S. Y. Choi and M. H. Jo, Identification of point defects in atomically thin transition-metal dichalcogenide semiconductors as active dopants, *Nano Lett.*, 2021, **21**, 3341–3354.

20 T. K. Rao, H. D. Wang, Y. J. Zeng, Z. N. Guo, H. Zhang and W. G. Liao, Phase transitions and water splitting applications of 2D transition metal dichalcogenides and metal phosphorous trichalcogenides, *Adv. Sci.*, 2021, **8**, 2002284.

21 S. S. Li, H. Wang, J. Wang, H. J. Chen and L. Shao, Control of light-valley interactions in 2D transition metal dichalcogenides with nanophotonic structures, *Nanoscale*, 2021, **13**, 6357.

22 Y. C. Lin, R. Torsi, D. B. Geohegan, J. A. Robinson and K. Xiao, Controllable thin-film approaches for doping and alloying transition metal dichalcogenides monolayers, *Adv. Sci.*, 2021, **8**, 2004249.

23 S. Wang, M. S. Ukhtary and R. Saito, Strain effect on circularly polarized electroluminescence in transition metal dichalcogenides, *Phys. Rev. Res.*, 2020, **2**, 033340.

24 Y. F. Zhang, J. B. Pan and S. X. Du, Geometric, electronic, and optical properties of MoS_2/WSSe van der Waals heterojunctions: a first-principles study, *Nanotechnology*, 2021, **32**, 355705.

25 X. T. Yu, X. Wang, F. F. Zhou, J. L. Qu and J. Song, 2D van der Waals heterojunction nanophotonic devices: from fabrication to performance, *Adv. Funct. Mater.*, 2021, **31**, 2104260.

26 S. Q. Hu, J. P. Xu, Q. H. Zhao, X. G. Luo, X. T. Zhang, T. Wang, W. Q. Jie, Y. C. Cheng, R. Frisenda, A. Castellanos-Gomez and X. T. Gan, Gate-switchable photovoltaic effect in BP/$MoTe_2$ van der Waals heterojunctions for self-driven logic optoelectronics, *Adv. Opt. Mater.*, 2020, **9**, 2001802.

27 H. D. Wang, S. Gao, F. Zhang, F. X. Meng, Z. N. Guo, R. Cao, Y. H. Zeng, J. L. Zhao, S. Chen, H. G. Hu, Y. J. Zeng, S. J. Kim, D. Y. Fan, H. Zhang and P. N. Prasad, Repression of Interlayer recombination by graphene generates a sensitive nanostructured 2d vdW heterostructure based photodetector, *Adv. Sci.*, 2021, **8**, 2100503.

28 R. C. Luo, W. W. Xu, Y. Z. Zhang, Z. Q. Wang, X. D. Wang, Y. Ga, P. Liu and M. W. Chen, Van der Waals interfacial reconstruction in monolayer transition-metal dichalcogenides and gold heterojunctions, *Nat. Commun.*, 2020, **11**, 1011.

29 L. Yuan, B. Y. Zheng, J. Kunstmann, T. Brumme, A. B. Kuc, C. Ma, S. B. Deng, D. Blach, A. Pan and L. B. Huang, Twist-angle-dependent interlayer exciton diffusion in WS_2-WSe_2 heterobilayers, *Nat. Mater.*, 2020, **19**, 617–623.

30 X. D. Guo, R. N. Liu, D. B. Hu, H. Hu, Z. Wei, R. Wang, Y. Y. Dai, Y. Cheng, K. Chen, K. H. Liu, G. Y. Zhang, X. Zhu, Z. P. Sun, X. X. Yang and Q. Dai, Efficient all-optical plasmonic modulators with atomically thin van der Waals heterostructures, *Adv. Mater.*, 2020, **32**, 1907105.

31 C. L. Tang, Z. W. Zhang, S. Lai, Q. H. Tan and W. B. Gao, Magnetic proximity effect in graphene/$CrBr_3$ van der Waals heterostructures, *Adv. Mater.*, 2020, **32**, 1908498.

32 K. S. Kamal, W. C. Lu, J. Bernholc and V. Meunier, Electron transport in multiterminal molecular devices: A density functional theory study, *Phys. Rev. B: Condens. Matter Mater. Phys.*, 2010, **81**, 125420.

33 M. W. Iqbala, K. Shahzada, H. Ateeqa, I. Aslamb, S. Aftabc, S. Azama, M. A. Kamrand and M. F. Khan, An effectual enhancement to the electrical conductivity of graphene FET by silver nanoparticles, *Diamond Relat. Mater.*, 2020, **106**, 107833.

34 Y. B. Hu, J. S. Yoo, H. T. Ji, A. Goodman and X. M. Wu, Probe measurements of electric field and electron density fluctuations at megahertz frequencies using in-shaft miniature circuits, *Rev. Sci. Instrum.*, 2021, **92**, 033534.

35 D. V. Gruznev, L. V. Bondarenko, A. Y. Tupchaya, V. G. Kotlyar, O. A. Utas, A. N. Mihalyuk, N. V. Denisov, A. V. Matetskiy, A. V. Zotov and A. A. Saranin, Atomic, electronic and transport properties of In-Au 2D compound on Si(100), *J. Phys.: Condens. Matter*, 2019, **32**, 135003.

36 N. Papadopoulos, E. Flores, K. Watanabe, T. Taniguchi, J. R. Ares, C. Sanchez, I. J. Ferrer, A. Castellanos-Gomez, G. A. Steele and H. S. J. van der Zant, Multi-terminal electronic transport in boron nitride encapsulated TiS_3 nanosheets, *2D Mater.*, 2019, **7**, 015009.

37 N. V. Denisov, A. V. Matetskiy, A. N. Mihalyuk, S. V. Eremeev, S. Hasegawa, A. V. Zotov and A. A. Saranin, Superconductor-insulator transition in an anisotropic two-dimensional electron gas assisted by one-dimensional Friedel oscillations: (Tl, Au)/Si(100)-$c(2 \times 2)$, *Phys. Rev. B: Condens. Matter Mater. Phys.*, 2019, **100**, 155412.

38 J. Q. Zhou, J. F. Qiao, C. G. Duan, A. Bournel, K. L. Wang and W. S. Zhao, Large tunneling magnetoresistance in VSe_2/MoS_2 magnetic tunnel junction, *ACS Appl. Mater. Interfaces*, 2019, **11**, 17647–17653.

39 H. Y. Zhou, Y. G. Zhang and W. S. Zhao, Tunable tunneling magnetoresistance in van der Waals magnetic tunnel junctions with 1T-$CrTe_2$ electrodes, *ACS Appl. Mater. Interfaces*, 2021, **13**, 1214–1221.

40 Y. L. Guo, Y. H. Zhang, Z. B. Zhou, X. W. Zhang, B. Wang, S. J. Yuan, S. Dong and J. L. Wang, Spin-constrained optoelectronic functionality in two-dimensional ferromagnetic semiconductor heterojunctions, *Mater. Horiz.*, 2021, **8**, 1323.

41 S. K. Behera and P. Deb, Spin-transfer-torque mediated quantum magnetotransport in MoS_2/phosphorene vdW heterostructure based MTJs, *Phys. Chem. Chem. Phys.*, 2020, **22**, 19139.

42 K. Miyajima, A. Nakajima, S. Yabushita, M. B. Knickelbein and K. Kaya, Ferromagnetism in one-dimensional vanadium-benzene sandwich clusters, *J. Am. Chem. Soc.*, 2004, **126**, 13202–13203.

43 M. Mitsui, S. Nagaoka, T. Matsumoto and A. Nakajima, Soft-landing isolation of Vanadium−Benzene sandwich clusters

on a room-temperature substrate using-alkanethiolate self-assembled monolayer matrixes, *J. Phys. Chem. B*, 2006, **110**, 2968–2971.

44 J. Wang, H. P. Acioli and J. Jellinek, Structure and magnetism of V_nBz_{n+1} sandwich clusters, *J. Am. Chem. Soc.*, 2005, **127**, 2812–2813.

45 S. Nagao, A. Kato and A. Nakajima, Multiple-decker sandwich poly-ferrocene clusters, *J. Am. Chem. Soc.*, 2000, **122**, 4221–4222.

46 X. Y. Liang, G. L. Zhang, P. Sun, Y. Shang, Z. D. Yang and X. C. Zeng, The electronic and transport properties of $(VBz)_n$@CNT and $(VBz)_n$@BNNT nanocables, *J. Mater. Chem. C*, 2015, **3**, 4039.

47 S. B. Desai, S. R. Madhvapathy, A. B. Sachid, J. P. Llinas, Q. Wang, G. H. Ahn, G. Pitner, M. J. Kim, J. Bokor, C. Hu, H. S. P. Wong and A. Javey, MoS_2 transistors with 1-nanometer gate lengths, *Science*, 2016, **354**, 99–102.

48 A. Antušek, M. Blaško, M. Urban, P. Noga, D. Kisić, M. Nenadović, D. Lončarevićd and Z. Rakočević, Density functional theory modeling of C–Au chemical bond formation in gold implanted polyethylene, *Phys. Chem. Chem. Phys.*, 2017, **19**, 28891–28906.

49 S. S. Li, H. Yu, G. L. Zhang and Y. Y. Hu, Four probe electron transport characteristics porphyrin phenylacetylene molecule devices, *New J. Chem.*, 2020, **45**, 2520–2528.

50 D. Jariwala, V. K. Sangwan, D. J. Late, J. E. Johns, V. P. Dravid, T. J. Marks, L. J. Lauhon and M. C. Hersam, Band-like transport in high mobility unencapsulated single-layer MoS_2 transistors, *Appl. Phys. Lett.*, 2013, **102**, 173107.

51 H. Yu, Y. Shang, L. Pei, G. L. Zhang and H. Yan, Spin-polarized gate tuned transport property of a four-terminal MoS_2 device: a theoretical study, *J. Mater. Sci.*, 2021, **56**, 11847–11865.

52 A. Nourbakhsh, A. Zubair, M. S. Dresselhaus and T. Palacios, Transport properties of a MoS_2/WSe_2 heterojunction transistor and its potential for application, *Nano Lett.*, 2016, **16**, 1359–1366.

53 L. T. Qu, Y. Liu, J. B. Baek and L. M. Dai, Nitrogen-doped graphene as efficient metal-free electrocatalyst for oxygen reduction in fuel cells, *ACS Nano*, 2010, **4**, 1321–1326.

54 Y. X. Wang, Y. J. Jiang, S. N. Gao, H. Yu, G. L. Zhang and F. M. Zhang, Tuning magnetism and transport property of planar and wrinkled FePP@GNR hybrid materials, *AIP Adv.*, 2020, **10**, 045112.

55 J. Taylor, H. Guo and J. Wang, Ab initio modeling of quantum transport properties of molecular electronic devices, *Phys. Rev. B: Condens. Matter Mater. Phys.*, 2001, **63**, 245407.

56 B. Wang, J. Wang and H. Guo, Ab initio calculation of transverse spin current in graphene nanostructures, *Phys. Rev. B*, 2009, **79**, 165417.

57 H. C. Lü, Y. Zhang, X. J. Liu, Y. Wang, Q. Zhang and H. T. Yin, Theoretical limit of how small we can make MoS_2 transistor channels, *J. Phys. D: Appl. Phys.*, 2022, **55**, 105304.

58 J. Junquera, Ó. Paz, D. Sánchez-Portal and E. Artacho, Numerical atomic orbitals for linear-scaling calculations, *Phys. Rev. B*, 2001, **64**, 235111.

59 X. Liu, Y. Z. Tan, Z. Y. Ma and Y. Pei, First-principles study of structural, electronic, and magnetic properties of one-dimensional transition metals incorporated vinylnaphthalene molecular wires on hydrogen-terminated silicon surface, *J. Phys. Chem. C*, 2016, **120**, 27980–27988.

60 I. Solovyev, N. Hamada and K. Terakura, t_{2g} versus all 3d localization in $LaMO_3$ perovskites (M = Ti–Cu): First-principles study, *Phys. Rev. B: Condens. Matter Mater. Phys.*, 1996, **53**, 7158–7170.

61 M. Büttiker, Y. Imry, R. Landauer and S. Pinhas, Generalized many-channel conductance formula with application to small rings, *Phys. Rev. B: Condens. Matter Mater. Phys.*, 1985, **31**, 6207–6215.

62 H. Wang, J. Zhou, X. J. Liu, C. B. Yao, H. Li, L. Niu, Y. Wang and H. T. Yin, Spin transport through a junction entirely consisting of molecules from first principles, *Appl. Phys. Lett.*, 2017, **111**, 172408.

63 T. Gan, G. L. Zhang, Y. Shang, X. H. Su, Z. D. Yang and X. J. Sun, Electronic and transport properties of the $(VBz)_n$@MoS_2NT nanocable, *Phys. Chem. Chem. Phys.*, 2016, **18**, 4385–4393.